Micro-scale extensional rheometry using hyperbolic converging/diverging channels and jet breakup

Citation: Keshavarz, Bavand, and Gareth H. McKinley. "Micro-Scale Extensional Rheometry Using Hyperbolic Converging/diverging Channels and Jet Breakup." Biomicrofluidics 10, no. 4 (July 2016): 043502. © 2019 AIP Publishing LLC

As Published: http://dx.doi.org/10.1063/1.4948235

Publisher: AIP Publishing

Persistent URL: http://hdl.handle.net/1721.1/119898

Version: Final published version: final published article, as it appeared in a journal, conference proceedings, or other formally published context

Micro-scale extensional rheometry using hyperbolic converging/diverging channels and jet breakup

Bavand Keshavarz[a)] and Gareth H. McKinley
Hatsopoulos Microfluids Laboratory, Department of Mechanical Engineering, Massachusetts Institute of Technology, Cambridge, Massachusetts 02139, USA

(Received 29 January 2016; accepted 15 April 2016; published online 25 May 2016)

Understanding the elongational rheology of dilute polymer solutions plays an important role in many biological and industrial applications ranging from microfluidic lab-on-a-chip diagnostics to phenomena such as fuel atomization and combustion. Making quantitative measurements of the extensional viscosity for dilute viscoelastic fluids is a long-standing challenge and it motivates developments in microfluidic fabrication techniques and high speed/strobe imaging of millifluidic capillary phenomena in order to develop new classes of instruments. In this paper, we study the elongational rheology of a family of dilute polymeric solutions in two devices: first, steady pressure-driven flow through a hyperbolic microfluidic contraction/expansion and, second, the capillary driven breakup of a thin filament formed from a small diameter jet ($D_j \sim O(100\,\mu\text{m})$). The small length scale of the device allows very large deformation rates to be achieved. Our results show that in certain limits of low viscosity and elasticity, jet breakup studies offer significant advantages over the hyperbolic channel measurements despite the more complex implementation. Using our results, together with scaling estimates of the competing viscous, elastic, inertial and capillary timescales that control the dynamics, we construct a dimensionless map or nomogram summarizing the operating space for each instrument. *Published by AIP Publishing*. [http://dx.doi.org/10.1063/1.4948235]

I. INTRODUCTION

Quantifying the elongational rheology of weakly viscoelastic fluids can help us understand the complex fluid dynamical behavior of such materials, which arises due to the coupling between microstructure and flow.[1,2] Mucus, saliva, synovial fluids, and blood are just a few representative examples of such fluids, and many of our vital physiological functions depend on the flow behavior or, in other words, the rheology of these microstructured biomaterials.[3–5] Similarly, in many important industrial applications such as paint coating, inkjet printing, emulsification, and anti-mist fuel combustion, the rheological properties of weakly viscoelastic liquids play a significant role.[6–9]

One important characteristic behavior of viscoelastic liquids is the resistance that the underlying microstructure exhibits to deformation in elongational flows. This resistance is characterized by the extensional viscosity, and the value of η_E for viscoelastic solutions can be several orders of magnitude higher than the corresponding shear viscosities.[10–13] In many biological and industrial applications such as flow of biological fluids through contractions and valves, the flow of liquid foodstuffs through orifices,[14] or atomization of paints in an air-spray nozzle, the kinematics of the flow is dominated by elongational deformation, leading to dramatic effects of the extensional rheological properties on the flow.

Extensional rheometry is an ongoing challenge for dilute viscoelastic liquids due to the difficulties in generating purely elongational flow fields.[11,13,15,16] In the last 20 years, specialized devices such as filament stretching instruments have been developed that can induce a

[a)]Electronic mail: bavand@mit.edu

local flow field in the fluid sample that is purely elongational; however, these instruments often fail to operate successfully for even moderately viscous liquids ($\eta \leq 0.1\,\mathrm{Pa\,s}$).[17,18] For lower viscosity systems, an instrument based on the analysis of capillary thinning and breakup of liquid filaments was first introduced by Entov and coworkers[19] and later developed extensively by McKinley and coworkers and others.[20–24] Capillary Breakup Extensional Rheometry (CaBER) has become a common method to study the elongational rheology of a wide range of dilute complex fluids.[25–28] However, conventional measurements from CaBER can be affected by fluid inertia and the dynamics of the end-plates. Limits on the separation speed of the end-plates and other inertia-related issues have dramatic adverse effects on conventional CaBER measurements for liquids with low viscosity and low elasticity. Rodd *et al.*[21] and more recently Keshavarz *et al.*[7] have shown that two dimensionless numbers capture the importance of viscous and elastic forces compared to capillary forces, and the relative magnitude of these groups determine the efficacy of CaBER measurements. These two numbers are known as the Ohnesorge number $Oh \equiv \eta_0/\sqrt{\rho R_0 \sigma}$ and Deborah number $De \equiv \tau_E/\sqrt{\rho R_0^3/\sigma}$, respectively.[29] Here, η_0 is the zero shear viscosity, ρ is the density, σ is the surface tension, and τ_E is the elongational relaxation time. In addition to material properties, it is clear that the geometry (R_0) of the rheometric device also plays a role in the relative importance of each effect. For liquids with Deborah and Ohnesorge numbers smaller than unity ($De \lesssim 1$ and $Oh \lesssim 1$), CaBER measurements are typically not possible due to the dominance of inertia effects. From a practical standpoint, this limits the ability of the instrument to measure the viscoelastic properties of liquids with $\tau_E \lesssim \sqrt{\rho R_0^3/\sigma}$. For $\rho \sim 10^3\,\mathrm{kg/m^3}$, $R_0 \sim 3\,\mathrm{mm}$, $\sigma \sim 60 \times 10^{-3}\,\mathrm{N/m}$, this gives a constraint of $\tau_E \lesssim 21\,\mathrm{ms}$. It is clear from these scalings that reducing the characteristic length scale of the test geometry (e.g., the initial radius of the liquid bridge in the CaBER instrument) into the microfluidic domain can help in minimizing the importance of inertial effects. These ideas have been introduced in a recent review[30] and are considered in more detail elsewhere in this special issue.[18] It is noteworthy that many other microfluidic techniques are available for extensional rheology with different mechanisms that benefit from either pressure drop measurements, flow-induced birefringence, or capillary pinch off in microfabricated channels with a range of different geometries.[31–37] Studying the details of all these devices is beyond the scope of our current study; however, a review by Haward[18] provides an overview of each of these methods.

Knowing the limits of the commercial CaBER instrument when measuring the extensional rheology of dilute solutions, several extensions and alternate protocols have been introduced in the literature. The Slow Retraction Method (SRM)[38] and Cambridge Trimaster[39,40] are devices similar to CaBER that also utilize capillary thinning but show a substantial improvement in the range of measured elongational relaxation times (down to $\tau_E \simeq 80\,\mu\mathrm{s}$). A more recent approach[7] has reintroduced an old concept based on studying the capillary breakup of a thin viscoelastic liquid jet. The technique, christened by the authors as Rayleigh Ohnesorge Jetting Extensional Rheometry (ROJER), is a contemporary adaptation of an idea originally introduced by Schümmer and Tebel.[41–43] Using ROJER, Keshavarz *et al.*[7] studied a family of dilute polymer solutions in both the linear and nonlinear regimes of jet deformations. The reported values of relaxation time extracted from jet rheometry tests for dilute polymer solutions were as low as $\tau_E \simeq 60\,\mu\mathrm{s}$.[7]

A different class of instruments for probing elongational properties of dilute solutions is based on steady flow of viscoelastic fluids through a contraction or a contraction/expansion.[18,30,44] Imposing a sudden contraction on a fully developed channel flow induces streamwise extensional kinematics that can cause significant stretching in the microstructure of the fluid, which then results in an extra pressure drop across the contraction/expansion. Essentially, this is the microfluidic analog of the "orifice plate" widely used for inline measurement of the flow rate of the Newtonian fluids (with constant rheology). Early studies of polymeric flows in contractions[45–51] showed many promising aspects and its relevance to commercial polymer processing operations such as injection molding established the contraction flow as a ubiquitous "rheological indexer" for elongational properties. Several recent studies,[52–56] benefiting from

advances in fabrication techniques for microfluidic channels, have focused on the flow of complex liquids in hyperbolic contraction geometries asserting that the hyperbolic profile will aid in maintaining the apparent stretch rate $\dot{\epsilon}_a$ constant throughout the contraction.[52,57] The recent study by Ober *et al.*[56] investigated a microfluidic hyperbolic expansion/contraction flow for a variety of different low viscosity test fluids and outlined methods based on two-dimensional lubrication theory to measure elongational properties based on pressure drop measurements across the contraction.

Considering the recent developments in microfluidic devices/flows for biological applications and the fact that many of the relevant liquids are of a weakly viscoelastic nature[30,44,58–62] it is important for the rheologist to develop a comprehensive understanding of the relative merits of different devices available for measuring the elongational rheology of dilute solutions. This situation is complicated by the knowledge that the extensional viscosity of a microstructured material is typically a time-varying function of both the strain rate $\dot{\epsilon}(t)$ and the total strain $\epsilon = \int_0^t \dot{\epsilon}(t')dt'$ imposed on a material element.[11,17] This can lead to difficulties in unambiguously determining the true extensional viscosity and in comparing results obtained with different instruments. Thus, in this study, we attempt to measure the elongational properties of a family of dilute polymer solutions by using two separate devices representing the different classes described above. Results from a microfluidic hyperbolic contraction device or "extensional viscometer-rheometer-on-a-chip" (EVROC), similar to the device used by Ober *et al.*,[56] are compared with jet breakup studies performed with the ROJER setup. This latter configuration focuses on the transient growth in the extensional viscosity for an unknown viscoelastic test sample at a single (nominally) constant strain rate that is set by the viscoelastic and interfacial properties of the fluid. In contrast, the former (EVROC) configuration considers a steady Eulerian flowfield with the total strain on a material element defined by the precise converging shape of the hyperbolic die and the 2D or 3D nature of the flowfield. In such an instrument, the strain rate can be systematically controlled by varying the flow rate through the device.

In this study, we highlight the limits of each device for quantitative measurements of the elongational properties of the fluid and develop simple physical scalings that can help elucidate the operational parameter space of each device. We represent our results in terms of an operating diagram or *nomogram* that delineates the regions of parameters where viscoelastic fluid properties can be successfully measured. The findings from this study provide practical guidance to microfluidic researchers who are interested in quantifying the elongational rheology of a wide range of industrial and biological liquids that exhibit weak viscoelastic behavior.

II. TEST FLUIDS AND EXPERIMENTAL SETUP

A. PEO solutions

In order to quantify the performance of the EVROC and ROJER configuration for extensional rheometry of weakly viscoelastic fluids, we prepared four different dilute polymeric solutions and monitored their flow behavior in hyperbolic channels (EVROC) and in the jet breakup process (ROJER). In addition to these four test fluids, we also tested a concentrated high molecular weight fluid in both the EVROC and CaBER devices to illustrate the similarities and differences when a markedly different viscosity range is probed. Table I summarizes the properties of all the test fluids. The viscoelastic fluids are prepared by dissolving small amounts of poly(ethylene oxide) (PEO) of three different average molecular weights (300 kg/mol, 1000 kg/mol, and 4000 kg/mol, respectively) in a 60–40 wt. % water-glycerol solvent ($\eta_s = 3.0$ m Pa s). The polymer overlap concentrations are, respectively, $c^* = 0.28\%$, 0.14%, and 0.08% for the 300 K, 1000 K, and 4000 K solutions. The values of c and L (the finite extensibility parameter) are estimated based on the scalings with average molecular weight that are evaluated by Haward *et al.*[32] for PEO solutions ($L \sim M_w^{1-\nu}$ in which $\nu = 0.56$ for a reasonably good solvent such as PEO in water-glycerol mixture).

It is known that at really high deformation rates, flexible polymer chains can be physically degraded due to their finite extensibility[63] and the viscoelastic behavior of many complex fluids decreases with time. Thus, for each ROJER or EVROC experiment, a fresh sample was used,

TABLE I. Properties of the viscoelastic test fluids. Different concentrations of poly (ethylene oxide) (PEO) at three different molecular weights were dissolved in the Newtonian solvent (60–40 wt. % Water + Glycerol $\eta_s = 3.0$ m Pa s). Definitions of the Deborah number (*De*), Ohnesorge number (*Oh*), Elasticity number (*El*), and Elasto-capillary number (*Ec*) that can be spanned by the fluids are described in the text.

M_w (K)	c (%)	c/c^*	η_0 (m Pa s)	τ_E (μs)	L	De	Oh	El	Ec
300	0.01	0.036	3.30	72	27	0.72	0.075	0.05	10
1000	0.01	0.07	3.40	425	50	4.5	0.075	0.34	60
4000	0.0025	0.03	3.10	957	100	10.5	0.075	0.79	140
4000	0.05	0.66	3.37	2045	100	21.9	0.095	2.07	232
4000	1	13.22	700	5.5×10^4	100	595	17	10.4×10^3	34

and the elapsed time gap between the EVROC and ROJER tests was kept to less than 30 min, in order to minimize the possibility of degradation between tests performed with different devices.

B. EVROC setup

The microfluidic planar hyperbolic contraction used in this study was fabricated by RheoSense (San Ramon, CA, USA).[64] The channel geometry and dimensions are shown in Figure 1(a). The channel height (h) is constant throughout the geometry. The flow upstream is pushed by a syringe pump through a straight channel region with constant width w_u to establish a fully developed shearing flow before reaching a symmetric contraction/expansion $0 \le x \le 2l_c$ in which the width varies as $w(x) = K/(x_0 - |x - l_c|)$, where $x_0 = l_c w_u/(w_u - w_c)$ and $K = l_c w_c w_u/(w_u - w_c)$. At an imposed flow rate Q, the average streamwise velocity at any plane x will vary as $\langle u(x)\rangle = Q/hw(x)$, so if we focus on the flow along the midplane of the device, the apparent extension rate $\dot{\epsilon}_a$ is

$$\dot{\epsilon}_a = \frac{Q}{l_c h}\left(\frac{1}{w_c} - \frac{1}{w_u}\right), \tag{1}$$

leading to a value of the average Hencky strain ϵ_H that is experienced by a fluid element following through the contraction given by

$$\epsilon_H(x) \equiv \int_0^{t(x)} \dot{\epsilon}_a dt', \tag{2}$$

where the limit of integration corresponds to the time at which the material element is at a location x along the constriction. This function reaches a maximum value of $\epsilon_H = \ln(w_u/w_c)$ when the material element reaches the throat of the contraction, $x = l_c$.

Before and after every test, the channels are flushed with water/ethanol to make sure that there is no residue from previous tests. For every measurement, the channel was filled with the test fluid for 10–15 min, and measurements are then started after pumping 3–5 ml of the sample through the EVROC fixture and monitoring the approach to steady state values for the pressure signal recorded by each transducer. Figure 1(b) shows the raw pressure measurements for one of the viscoelastic test solutions (PEO-4000 K-0.05 wt. %). The pressure drop across the hyperbolic contraction ΔP_c is evaluated from the pressure difference measured between the 2nd and 3rd sensors ΔP_{23} with a minor extrapolation upstream and downstream of the pressure transducers to correct for the fact that they are not located exactly at the throat entrance/exit of the converging/diverging region.[56] From Equations (1) and (2), it is clear that by varying the flow rate in the channel the apparent extension rate in the constriction is controlled, and measuring the pressure drop across the contraction then gives a direct measure of the viscoelastic effects involved in the deformation of material elements as they flow through the contraction/expansion.

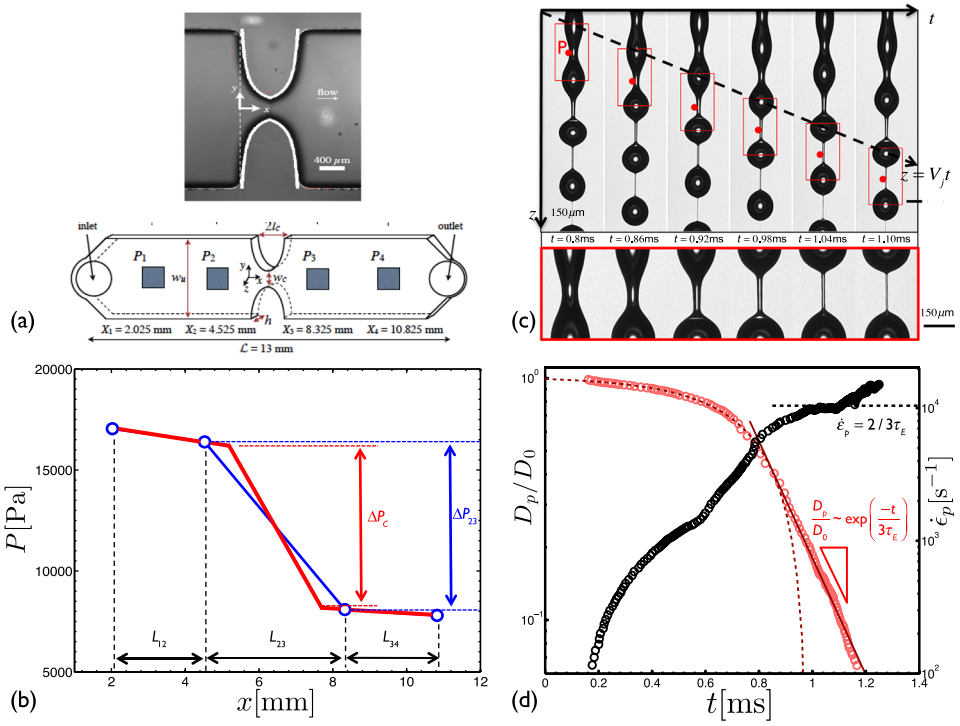

FIG. 1. (a) SEM image of the hyperbolic contraction and the dimensions of the entire geometry. Reproduced with permission from Ober *et al.*, Rheol. Acta **52**, 6 (2013). Copyright 2013 Springer. (b) Pressure measurements, for the PEO-4000 K–0.05wt. % solution. Four flush-mounted pressure transducers are located along the channel axis. The magnitude of the pressure drop across the contraction/expansion between sensors 2 and 3 (ΔP_c) is an indication of elongational effects. (c) Snapshots of a dilute PEO solution (PEO-300 K–0.05 wt. %) breaking up from a cylindrical liquid jet into spherical droplets as a consequence of Rayleigh-Plateau instability. A red box translating with a Lagrangian element P is plotted following a filament connected between two neighboring beads. The time evolution of the filament is recorded at 2.1 μm/pix and 10^4 frames/s. Reproduced with permission from Keshavarz *et al.*, JNNFM **222**, 171 (2015). Copyright 2015 Elsevier. (d) Diameter of a fixed Lagrangian point (e.g., the point P located at the bottom of the trough shown in (c)) is recorded and shown in a dimensionless form $D_p(t)/D_0$ where D_0 is the diameter of the jet right after exiting the nozzle (red data points). The dashed red line shows the evolution of the filament diameter predicted by linear stability analysis and the solid red line shows the theoretical prediction for the filament diameter in the elasto-capillary regime (corresponding to an exponential decay in diameter with time (Equation (3)). Using Equation (10) the local strain rate $\dot{\varepsilon}_p$ for a Lagrangian point P is also calculated and plotted versus time (black data points).

C. ROJER setup

The ROJER instrument used in this study is a bespoke apparatus that has been developed for elongational rheometry of very dilute polymeric liquids. The idea originates with Schümmer and Tebel,[41] and the details of the current ROJER instrument are extensively discussed by Keshavarz *et al.*[7] in their study of elongational effects on atomization of polymer solutions. A liquid jet is pushed at volumetric flow rate Q through a cylindrical tube that is periodically perturbed by radial squeezing induced by a piezoelectric actuator. The jet is then discharged into air through a small diameter ($2R_0 = 175\mu$m) ceramic precision nozzle. The jet is simultaneously illuminated by a strobe LED at a frequency $f - \Delta f$ that is slightly less than the frequency f of the piezoelectric actuator. This leads to the well-known stroboscope effect that allows us to capture movies with both high spatial and temporal resolutions (for more details on the relationship between $f, \Delta f, Q$, and R_0, see the detailed Appendix in Keshavarz *et al.*[7]). The resulting disturbances led to a small perturbation in the jet profile, $R(z, t)$, which grow with time as the jet travels downstream. This convective instability for Newtonian liquid jets has been known for many years and is typically referred to as Rayleigh-Plateau instability.[65,66] A linear stability analysis shows that for a given radius R_0, jet velocity $V_j = Q/\pi R_0^2$ and frequency of

perturbation f, a specific range of dimensionless wave-numbers $0 \leq kR_0 = 2\pi fR_0/V_j \leq 1$ have positive growth rates, and thus, the jet is unstable to linear perturbation with wave-numbers in this range.

Figure 1(c) shows how the imposed perturbation at the nozzle leads to a wave-like profile in the jet radius that grows in amplitude downstream. The early stages of the disturbance growth can be compared with the predictions from linear instability for the viscoelastic jet ($De = 0.72, Oh = 0.075, kR_0 = 0.8$), and the red dashed line in Figure 1(d) shows the prediction of linear instability theory[7,67] compared with the measured filament diameter at early times. As the Rayleigh-Plateau instability grows with time, the filament radius in a neck locally decreases, and the capillary pressure correspondingly increases. Concomitantly, the stretch rate $\dot{\epsilon}_p$ in the filament neck dramatically increases and the corresponding elongational stresses become increasingly dominant over inertia and viscous stresses in the thinning thread. In this regime, a balance emerges between the capillary pressure (which is the driving mechanism for the instability) and the elastic stresses (excited from the high deformation rate stretching flow imposed on the microstructure within the fluid). This regime is known as the elasto-capillary regime.[22] Using a canonical frame-invariant constitutive equation such as the Oldroyd-B model, it can be shown that the filament diameter in the elasto-capillary regime thins down with time in an exponential manner[22,68]

$$D_p(t)/D_0 = (GD_0/2\sigma)^{1/3} \exp(-t/3\tau_E), \tag{3}$$

where $D_0 \cong 2R_0$ is the initial diameter of the filament, σ is the surface tension of the liquid-air interface, G is the elastic modulus of the polymer in solution ($G = nkT$ for dilute solutions), and τ_E is the viscoelastic relaxation time for the fluid that appears in the Oldroyd-B model.

In the elasto-capillary regime, it is clear from Equation (3) that the filament diameter decays exponentially in time and the local stretch rate in a material element $\dot{\epsilon}_p = -2\dot{D}_p/D_p$ becomes constant at a value of $\dot{\epsilon}_p = 2/3\tau_E$. Figure 1(d) shows that in the ROJER experiment, the filament indeed locally forms a uniform cylindrical column that decreases in diameter with time exponentially and has a constant stretch rate, until the very final stages of the breakup process when the polymer chains reach their finite extensibility. Using this observation, one can easily measure the viscoelastic relaxation time of a low viscosity complex fluid by recording the thinning dynamics extracting the filament diameter $D_p(t)$ associated with a Lagrangian point of fixed identity P, and fitting the process to Equation (3). Thus, the ROJER device is in many ways similar to other conventional capillary-based extensional rheometers (such as the CaBER), and one can think of it as a "flying CaBER" with a sample that is convected downstream with the jet velocity V_j. However, the smaller initial sample dimensions in ROJER ($D_0 = 175\,\mu$m in ROJER as compared to $D_0 = 6$ mm typically in CaBER) coupled with the absence of issues associated with the initial acceleration of the plates in the CaBER device allows us to measure relaxation times in the ROJER device that are much smaller than the known limits of conventional CaBER measurements.[7,21]

III. MEASUREMENTS AND RESULTS

A. Shear viscosity

Before characterizing the elongational properties of the test fluids (with composition shown in Table I) by both EVROC and ROJER instruments, we performed a series of tests with a commercial stress-controlled rheometer (DHR-3 from TA Instruments New Castle DE) in a double-wall Couette geometry (inset image in Figure 2(a)) to characterize the shear rheology of each fluid. Measurements were performed over a wide range of shear rates. The limits of the shear viscosity measurements are set by the minimum torque ($\mathcal{T}_{\min} = 0.05\,\mu$N m) that the instrument can control/measure at lower rates and the maximum strain-rate is set by the onset of inertially induced secondary flows in the Couette cell. The inner cup has a 28.0 mm diameter, the rotor has an inner diameter of 29.5 mm and an outer diameter of 32 mm, and the outer cup is 34 mm in diameter.

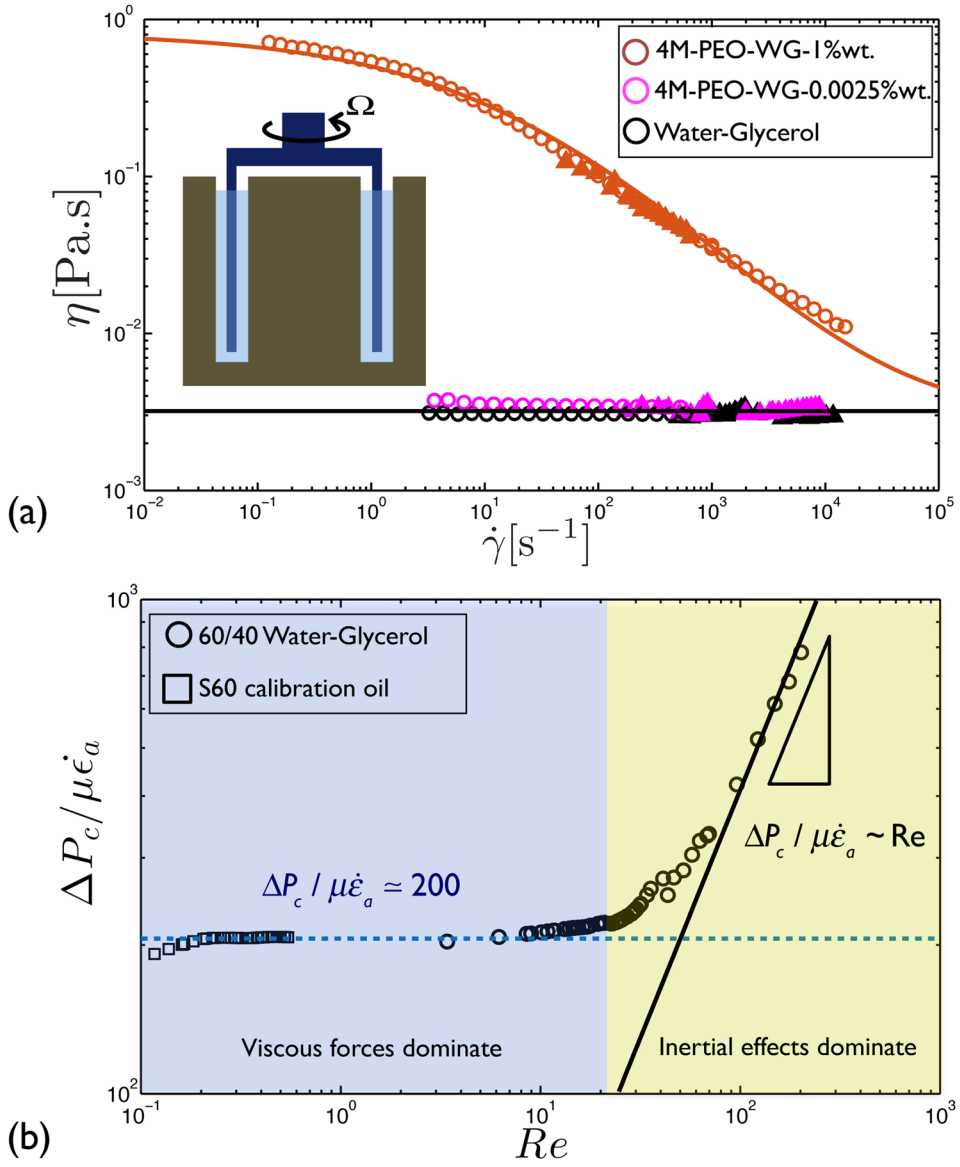

FIG. 2. (a) Shear viscosity measurements plotted for three different test fluids: the Newtonian solvent (○ and ▲), 4 M-PEO-0.0025 wt. % (magenta open circles and magenta filled triangles) and 4 M-PEO-1 wt. % (orange open circle and orange filled triangle). Open circles are data measured in a double-wall Couette geometry and the filled triangles are shear viscosity measurements from the EVROC device calculated from the measured pressure difference upstream between sensors 1 and 2. (b) Pressure difference across the hyperbolic contraction ΔP_c measured at different flow rates and plotted in a dimensionless form ($\Delta P_c/\mu\dot{\epsilon}_a$) vs. Reynolds number Re for different Newtonian liquids: S60 calibration oil (□) and water-glycerol solvent (60–40 wt. %) (○).

Figure 2(a) shows the results for the shear viscosity measured for the Newtonian solvent (black symbols) and two of the viscoelastic solutions formulated from 4000 K PEO at both a very low concentration $c/c^* = 0.03$ (magenta symbols) and also at a much higher concentration $c/c^* = 13.22$ (orange symbols). Open circles show results from the double-wall Couette geometry and the filled triangles show results from EVROC measurements. The microfluidic chip can be used to determine the shear viscosity of the fluid by focusing only on the pressure difference measured between sensors 1 and 2 which are located in the region of steady fully developed channel flow before the hyperbolic contraction. Assuming a fully developed 2D flow, it is known that the wall shear stress Σ_w is related to the pressure drop ΔP_{12} between the two upstream flush-mounted sensors by the expression:[64]

$$w_u h \Delta P_{12} = 2L_{12}(w_u + h)\Sigma_w. \tag{4}$$

At the same time, for a given flow rate Q imposed by the syringe pump, the apparent shear rate can be calculated as $\dot{\gamma}_a = 6Q/w_u h^2$. However, to determine the true wall shear rate which captures the effects of shear-thinning fluid rheology on the velocity profile, we use the Weissenberg-Rabinowitsch-Mooney (WRM) equation[10,64,69]

$$\dot{\gamma}_{true} = \frac{\dot{\gamma}_a}{3}\left[2 + \frac{d(\ln\dot{\gamma}_a)}{d\ln(\Sigma_w)}\right]. \tag{5}$$

Using Equations (4) and (5) for a given flow rate, knowing the channel geometry and the pressure drop between the first two sensors ΔP_{12}, one can calculate the true shear viscosity $\eta(\dot{\gamma}_{true}) \equiv \Sigma_w/\dot{\gamma}_{true}$ at each imposed shear rate.

As shown in Figure 2(a), the values of the shear viscosity obtained from the EVROC microfluidic device are in good agreement with the measured values from the double-wall geometry in the conventional stress-controlled rheometer. The results for the very dilute solutions ($c/c^* \ll 1$) show very little difference from the solvent viscosity, but for the higher concentration, a pronounced shear thinning behavior can be observed (brown data). The data for the high concentration PEO solution are fitted by a Carreau-Yasuda model[69]

$$\frac{\eta - \eta_s}{\eta_0 - \eta_s} = \left[1 + (\tau_s\dot{\gamma})^a\right]^{(n-1)/a}, \tag{6}$$

where η_0 and η_s are, respectively, the zero shear-rate and solvent viscosity, τ_s is a timescale that sets the onset of shear thinning at $\dot{\gamma}^* \simeq 1/\tau_s$, $n-1$ sets the power law slope and a sets the breadth of the transition region. Fixing $\eta_0 = 0.8\,\text{Pa s}, \eta_s = 0.003\,\text{Pa s}$ and also setting the value of τ_s to be equal to the relaxation time measured in the capillary breakup experiment (described below) $\tau_s = \tau_E = 55$ ms, one can see that a good fit of the model (solid line in Figure 2(a)) can be obtained with $n = 0.3$ and $a = 0.4$.

B. Elongational viscosity

1. EVROC measurements

As mentioned before, one signature of elastic effects in converging flows of a complex fluid is the enhanced pressure drop across the contraction.[45,48,56] However, extra care must be taken in interpreting the extra pressure drop because of additional effects arising from viscous stresses, inertia and the unsteady nature (in a Lagrangian sense) of the flow experienced by a material element flowing through the hyperbolic contraction. Connecting the measured pressure drop to the true extensional viscosity is a known challenge in microfluidic extensional rheometry.[30,70,71]

One of the major complications is related to the nonlinear effects of fluid inertia. Figure 2(b) shows the pressure drop ΔP_c across the hyperbolic contraction measured for different Newtonian fluids over a wide range of Reynolds numbers. The Reynolds number on the abscissa is defined as $Re \equiv \rho d_h l_c \dot{\epsilon}_a/\eta_0$, where ρ is the fluid density, η_0 is the zero shear viscosity (in case of Newtonian liquids $\eta_0 = \mu$), $l_c\dot{\epsilon}$ is the local increment in velocity at the throat arising from the constriction, and $d_h = 2hw_c/(h + w_c) = 267\,\mu$m is the hydraulic diameter defined at the throat of the contraction. The true pressure drop across the contraction ΔP_c is related to the measured pressure difference between sensors 2 and 3 by the expression[56]

$$\Delta P_c = \Delta P_{23}\left\{1 - \frac{1}{2}\left(\frac{1}{\mathcal{P}} - 1\right)\frac{L_{23} - 2l_c}{L}\right\}, \tag{7}$$

where $L_{23} = 3.8$ mm, $L = L_{12} = L_{23} = 2.5$ mm, $l_c = 400\,\mu$m are properties of the specific geometry and the fraction of the total pressure drop across the device that arises from the converging/

diverging flow is denoted $\mathcal{P} = \Delta P_{23}/\Delta P_{14}$. Simple scaling arguments show that, for Newtonian liquids, in the limit of very low Re, the pressure drop will scale with the viscous stress $\Delta P_c \sim \mu\dot{\epsilon}_a$, and at high Re, inertial effects will dominate so that the pressure drop should scale with the inertially induced stresses in the liquid $\Delta P_c \sim \rho V^2 \sim \rho(Q/wh)^2$. The Newtonian data in Figure 2(b) show a similar trend; at low Re, the dimensionless pressure drop in the device normalized by a characteristic viscous stress is constant at a value set by the geometric dimensions of the channel[56] $\Delta P_c/\mu\dot{\epsilon}_a \sim 200$, and at high Re numbers, the normalized pressure drop scales linearly with Reynolds number $\Delta P_c/\mu\dot{\epsilon}_a \sim Re$, suggesting that for high Reynolds number flows, enhancements in the pressure drop measured across the contraction do not arise from the extensional viscosity but rather from fluid inertia. For the specific geometry used in this study, transition between the viscous- and inertia-dominated regions occurs at $Re_c \sim O(10)$, consistent with the separate study by Ober *et al.*[56]

Because of the nonlinear inertial effects at high Reynolds numbers ($Re \geq O(10)$), it is clear that proper extensional rheometry measurements are not possible in this limit (yellow shaded area in Figure 2(b)). Analyzing the pressure drop data above this limit and connecting that to the elongational properties of a liquid can be very misleading.[71] In the same way, increases in the torque measured in a Taylor-Couette device at high shear rates may be erroneously interpreted as shear thickening in the fluid rheology when it in fact arises from secondary flows. If a strongly extensionally thickening fluid is analyzed, it may result in true elastically dominated increases in the pressure drop before these inertial effects set in at $Re \sim O(10)$. However, one can imagine that for many weakly elastic fluids, the critical strain rate at which elongational rheological properties start to dominate over inertial effects may be high enough that, in a device such as EVROC, the corresponding values of Re would approach the limit of inertially dominated flows. Thus, the response of the unknown material in this range of strain rates would be a mixture of inertial and elastic effects. Decoupling these effects from one another is hard, if not impossible.

In order to probe the sensitivity limit of EVROC, we tested the 60–40 wt. % water-glycerol solvent (Table I) along with one concentrated and four dilute PEO solutions. Figure 3(a) shows a summary of these data. Preliminary results for all of the fluids are plotted in terms of normalized pressure drop measured at different values of Re. It is clear that, within the operational limits of EVROC ($Re \leq Re_c$), for the three most dilute solutions (green, blue, and magenta data points), the normalized pressure drop is indistinguishable (within the experimental limits) from the corresponding values for the Newtonian solvent. Subtle differences emerge for some of these solutions at higher strain rates but the onset of these distinctions lie in the region where the pressure drop data are already polluted by inertial effects (yellow-shaded area). For the most dilute and lowest molecular weight PEO solution (300 K–0.01 wt. %), the measured pressure drop values remain indistinguishable from the Newtonian solvent even up to the upper limit of flow rates ($Q_{\max} = 15.2$ ml/min; $\dot{\gamma}_a = 1.2 \times 10^4$ s^{-1}) achievable by the syringe pump (compare the black and green symbols in Figure 3(a)).

It is only for the two solutions with higher concentrations of 4000 K PEO (red and orange data points) that measurable differences from the Newtonian solvent emerge before inertia effects start to dominate. The data for the 4000 K–0.05% solution (red symbols) show the onset of extensional thickening at a critical extension rate, as expected for dilute polymer solutions. Interestingly, the data for the 4000 K–1 wt. %. solution (orange symbols) show a relatively constant value for the pressure drop across the contraction/expansion, which is an order of magnitude higher than the corresponding asymptotic value for the inertia-less Newtonian limit (dashed black line). The relaxation time for this fluid $\tau_E \sim 55$ ms is high enough that even at the very lowest flow rates tested in the EVROC device $Q \simeq 0.05$ ml/min corresponding to $\dot{\epsilon} \simeq 20\,\text{s}^{-1}$ the induced stretch rate is higher than the relaxation rate of the microstructure $\dot{\epsilon} \geq 1/2\tau_E$. Thus, the viscoelastic contribution to the pressure drop dominates over viscous effects and leads to the enhanced pressure drop across the contraction for all test conditions.

This dataset shows that although the EVROC has clear potential for measuring the extensional properties of sufficiently viscoelastic solutions, there also exists a certain group of weakly viscoelastic liquids for which EVROC measurements, if not completely impossible, are

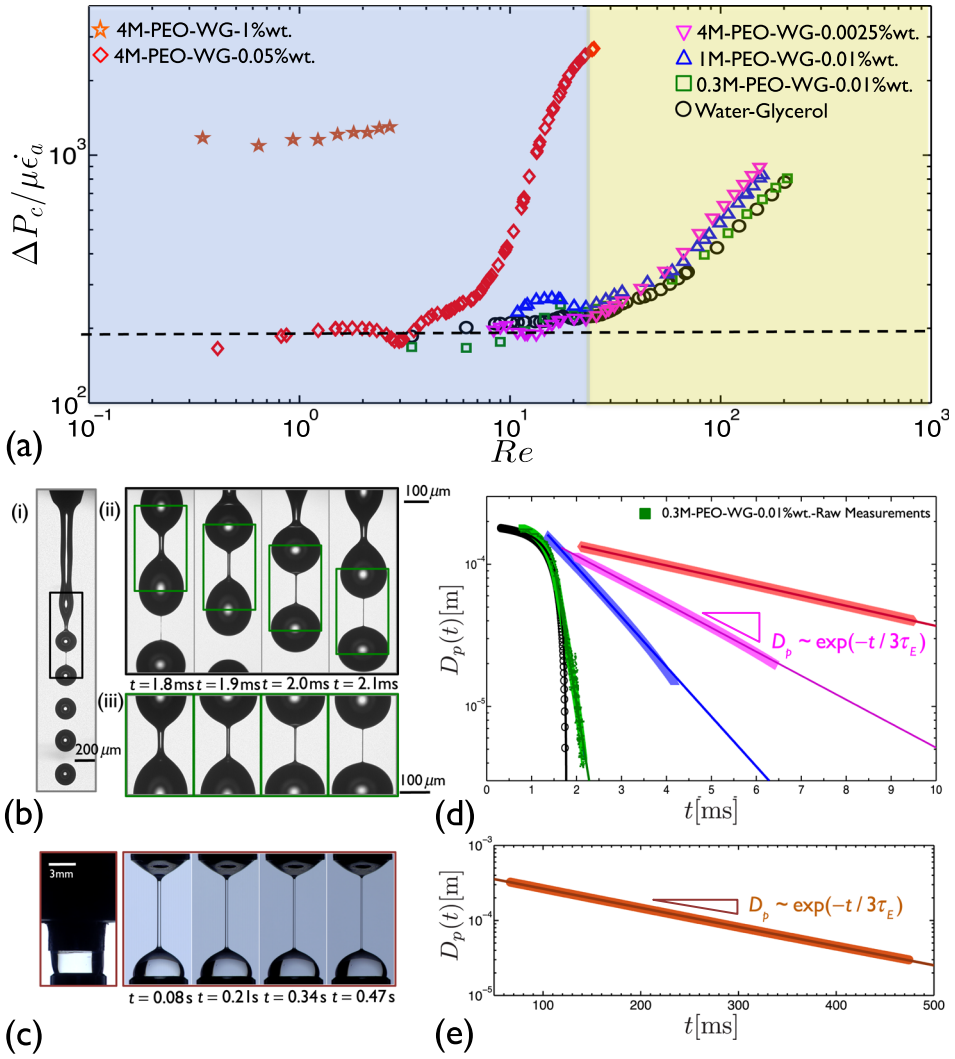

FIG. 3. (a) Pressure drop across the hyperbolic contraction in EVROC tests measured at different flow rates and plotted in a dimensionless form, $\Delta P_c/\mu\dot{\epsilon}_a$ versus Re, for different fluids: the Newtonian solvent (○), 300 K-PEO-0.01 wt. % (green squares), 1000 K-PEO-0.01 wt. % (blue triangles), 4000 K-PEO-0.0025 wt. % (magenta inverted triangles), 4000 K-PEO-0.05 wt. % (red diamonds), 4000 K-PEO-1 wt. % (orange stars). (b) Snapshots of the jet breakup process for the 300 K-PEO-0.01 wt. % solution in the ROJER setup: (i) An image of the entire process showing the jet exiting the nozzle and breaking up into individual droplets. (ii) A time sequence of enlarged snapshots showing the emergence of a cylindrical filament that can be followed by the Lagrangian box (in green) that is moving downstream with the jet velocity. (iii) Time evolution of the filament in the Lagrangian box shows elasto-capillary thinning. (c) Snapshots demonstrating the elasto-capillary thinning regime in the CaBER device for the 4000 K-PEO-1 wt. % solution. (d) Time evolution of the filament neck diameter $D_p(t)$ is plotted for different fluids tested in the ROJER setup: the Newtonian solvent (○), 300 K-PEO-0.01 wt. % (green squares), 1000 K-PEO-0.01 wt. % (blue triangles), 4000 K-PEO-0.0025 wt. % (magenta inverted triangles), 4000 K-PEO-0.05 wt. % (red diamonds). (e) Results from CaBER test for the 4000 K-PEO-1 wt. % solution (orange circles). Solid lines in both (d) and (e) show fits of the exponential decay expected from theory (Equation (3)). Raw measurements of $D_p(t)$ for the 300 K-PEO-0.01 wt. % solution (green filled squares) are also plotted, to provide an indication of typical fluctuations in the diameter measurments.

at least heavily polluted by inertia effects. In Section III, we quantify the dimensionless criteria that delineate these different regions.

2. ROJER measurements

In order to seek an alternative method for probing the extensional rheology of dilute solutions, we studied the behavior of all of the test fluids using capillary thinning and jet breakup. For the very concentrated PEO solution (4000 K–1 wt. %), the test liquid was sufficiently elastic that measurements could be performed with a conventional CaBER device. As a result of

their very low shear viscosities, measurements for the Newtonian solvent and the other four dilute polymer solutions were carried out using our ROJER setup described in Section II C.

In Figure 3(b-i), we show a snapshot of the viscoelastic jet for the 300 K–0.01 wt. % solution at $Q = 4$ ml/min corresponding to $V_j = 1.4$ m/s. Due to the small dimension of the jet ($D_0 \simeq 175\,\mu$m), the entire jet breakup process happens in a remarkably small length ($l_{break-up} \sim O(1\,\text{mm})$) and time scales ($t_{break-up} \sim l_{break-up}/V_j \sim (O(1\,\text{ms}))$. Using a macro imaging lens, one can optically zoom and magnify the image (up to a certain optical limit that depends on the magnification and numerical aperture of the lens) to gain a better view of the region of interest, which corresponds to the region from the onset of filament formation till the jet breaks up into discrete droplets. The black rectangle in Figure 3(b-i) indicates this region and a time series of the optically zoomed view of this region (with a resolution of approximately $2\,\mu$m/pixel) are shown in Figure 3(b-ii). As is clear from Figure 3(b-ii), the thinning dynamics of a Lagrangian element which is moving downstream with jet velocity V_j (e.g., elements inside the green box) can be tracked accurately and the evolution in filament diameter for a fixed Lagrangian point P are recorded with time in the same way as for the CaBER instrument (Figure 3(b-iii)).

The results are plotted in terms of the filament diameter $D_p(t)$ for the neck region in Figure 3(d) (raw measurements of the filament diameter are first smoothened by a moving average scheme from Matlab and then plotted). It is clear that for all dilute solutions tested with ROJER the thinning filaments exhibit an elasto-capillary regime at intermediate times in which the diameter decays with time exponentially (Equation (3)). This is significantly different from the trend that is observed for the Newtonian solvent (black circles). The data for the Newtonian solvent follow the predictions of the initial linear instability analysis (solid black line, see Keshavarz *et al.*[7] for details) for almost the entire observable window and only show a narrow visco-capillary balance in the final stages of breakup. When compared to the Newtonian data, even the very dilute 300 K–0.01 wt. % solution (green symbols) shows a clear deviation in the diameter evolution with time and the final stages of breakup show an exponential decay in diameter consistent with the elasto-capillary balance (see the supplementary material for more details).[72] For the concentrated solution (4000 K–1 wt. %), the pressure drop required to force the fluid through the jet nozzle and piezo-tube is too large for the syringe pump. However, the fluid is sufficiently viscous that CaBER measurements could be performed and the results are shown in Figures 3(c) and 3(e). Due to the much higher relaxation time for this concentrated solution, the duration of the capillary breakup event is resolvable using CaBER measurements ($t_{break-up} \geq O(0.1\,\text{s})$).

C. Analysis

1. EVROC data

To convert the pressure drop ΔP_c measured in the EVROC tests into a rheologically meaningful quantity such as the extensional viscosity, one has to isolate the viscoelastic contribution of the pressure drop. As discussed, the nonlinear effects of inertia for $Re \geq Re_c$ make this complicated, and it is recommended to measure the pressure drops in the limit of negligible inertia ($Re \leq Re_c$). However, even for measurements performed in the viscous-dominated regime one must be cautious in analyzing experimental pressure drop data. For inertialess flows of viscoelastic liquids, the calculated pressure drop across the contraction has two main components that we decompose additively so that $\Delta P_c = \Delta P_e + \Delta P_v$, where ΔP_e is the viscoelastic component of interest for computing the elongational viscosity and ΔP_v is a viscous component due to shearing at the walls.[46,47,56] In order to measure/calculate elastic component ΔP_e one needs to have an accurate expression for the viscous component ΔP_v. For a non-Newtonian fluid sample, this can be done by considering the flow of an inelastic fluid such as a phenomenological power law model (for which $\eta = m\dot{\gamma}^{n-1}$).[10] An analytical expression for the viscous pressure drop across the hyperbolic contraction using a power-law model ($\Delta P_{c,v}^{PL}$) is given by Ober *et al.*[56]

$$\Delta P_{c,v}^{PL} = \frac{2^{n+2}}{n+1}\left(\frac{2n+1}{n}\right)^{n}\left(\frac{l_c}{h}\right)^{n+1}\left\{\left(\frac{w_u}{w_u - w_c}\right)^{n+1} - \left(\frac{w_c}{w_u - w_c}\right)^{n+1}\right\} m\dot{\epsilon}_a^n. \tag{8}$$

From the measured shear rheology shown in Figure 1, we can thus calculate $\Delta P_e = \Delta P_c - \Delta P_{c,v}^{PL}$. To connect the remaining pressure drop $\Delta P_e(Q)$ to the extensional viscosity, first Collier *et al.*[73] (for a semi-hyperbolic converging die) and later Ober *et al.*[56] (for the EVROC device used in this study) show that by assuming an incompressible flow and using a simple energy dissipation argument one can connect the rate of work done by the pressure drop occurring across the contraction to the viscous losses induced by extensional stress differences in the fluid. After some simplifications, the following expression for an ideal planar elongational flow is suggested by Ober *et al.*[56] for measuring the apparent extensional viscosity in a microfluidic contraction device at each imposed strain rate

$$\eta_{E,app.}^{+}(\dot{\epsilon}_a, \epsilon_H) = \frac{1}{\epsilon_H}\frac{\Delta P_e}{\dot{\epsilon}_a} = \frac{1}{\epsilon_H}\frac{\left(\Delta P_c - \Delta P_{c,v}^{PL}\right)}{\dot{\epsilon}_a}. \tag{9}$$

2. ROJER data

In EVROC measurements, one adjusts the imposed extensional deformation rate by controlling the flow rate through the device and then monitors the extensional stress difference that develops in the fluid by recording the pressure drop across the contraction. This is different from the corresponding measurement procedure and analysis appropriate for devices based on capillary thinning such as ROJER or CaBER. As the filament thins under the action of capillarity, the normal stress difference in the thinning thread balances with the capillary pressure which is naturally set by the surface tension so that $(\Sigma_{zz} - \Sigma_{rr}) = 2\sigma/D(t)$. The thinning filament is being elongated with a local stretch rate that can be measured by analyzing the time evolution of the filament diameter

$$\dot{\epsilon}_p = \frac{-2}{D_p(t)}\frac{dD_p}{dt}. \tag{10}$$

This allows us to calculate the local transient extensional viscosity of the fluid at each instant

$$\eta_{E,app}^{+} = \frac{-\sigma}{dD_p/dt}. \tag{11}$$

This material function thus varies with both imposed strain $\epsilon = \int_0^t \dot{\epsilon} dt'$ as well as the strain rate in the filament at that instant in time. In the elastocapillary thinning regime (given by Equation (3)), the strain rate is in fact constant. This can be directly verified by substituting Equation (3) in Equation (10) to give $\dot{\epsilon_p} = 2/3\tau_E$. In this region we thus expect the apparent extensional viscosity approaches the true material function expected in a homogeneous extensional flow.

Figure 4(a) shows a plot of the apparent extensional viscosity for all of the dilute polymer solutions studied (the 4000 K–1 wt. % solution with $c/c^* = 13.2$ is clearly not in the dilute regime, and since the primary focus of our study is on weakly viscoelastic fluids we postpone a discussion on the extensional rheology of this entangled semi-dilute solution to the supplementary material[72]). The circles show data analyzed from ROJER tests, and the red triangles are the EVROC results for the 4000 K–0.05 wt. % solution. Equations (10) and (11) are used to calculate the stretch rate and apparent elongational viscosity for ROJER tests,[74] and Equations (1) and (9) are used to calculate the values of average stretch rate and apparent extensional viscosity from the corresponding values of flow rate and pressure drop across the contraction in the EVROC test. Our results are also compared with the predictions of the FENE-P (finitely extensible nonlinear elastic) model, assuming the Peterlin statistical closure for the restoring force[10,75] (solid lines in both Figures 4(a) and 4(b)). Unlike simpler constitutive equations such

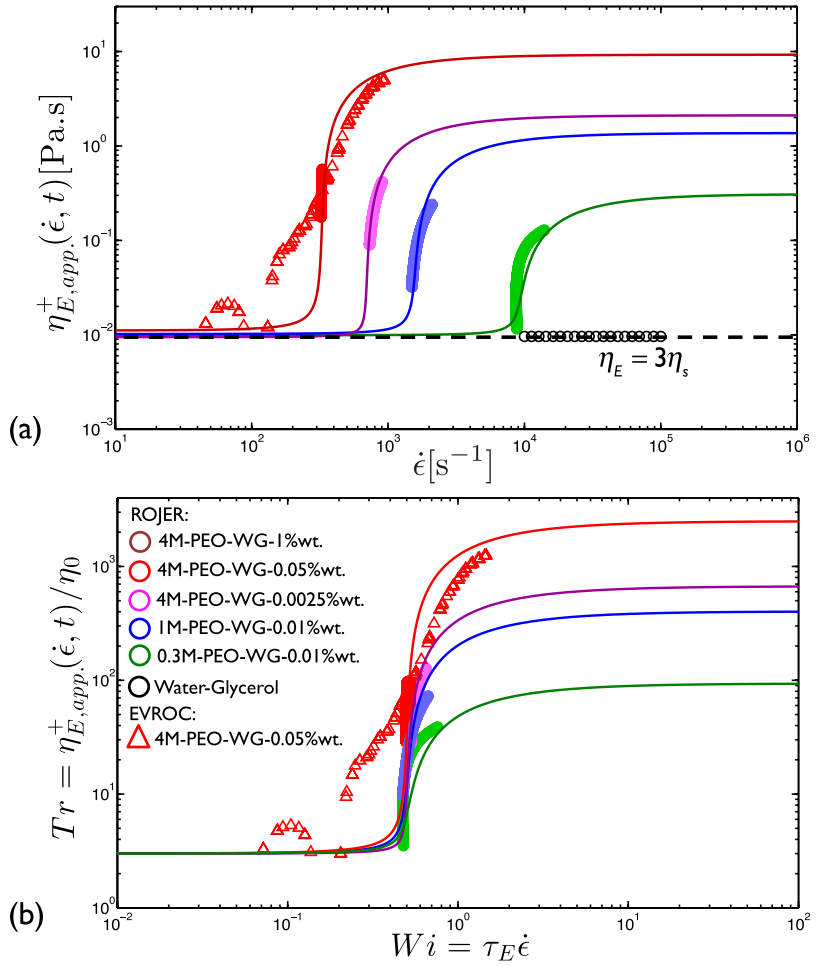

FIG. 4. (a) Circles show the apparent extensional viscosities measured from ROJER experiments for the Newtonian solvent (○), 300 K-PEO-0.01 wt. % (green circles), 1000 K-PEO-0.01 wt. % (blue circles), 4000 K-PEO-0.0025 wt. % (magenta circles), and the 4000 K-PEO-0.05 wt. % (red circles) solutions. Open triangles show the EVROC measurements for the 4000 K-PEO-0.05 wt. % solution (red triangles). The solid lines are predictions of FENE-P theory plotted for each liquid with the corresponding parameters from Table I. (b) Same data shown in (a) but plotted in dimensionless form: Trouton ratio $Tr \equiv \eta^+_E(\epsilon,\dot{t})/\eta_0$ versus the Weissenberg number $Wi \equiv \tau_E\dot{\epsilon}$.

as the Oldroyd-B model, which treats the polymer chains as ideal Hookean springs that are infinitely extensible, the FENE-P model assumes that the macromolecules have a finite extensibility and, once they are stretched to this fully unraveled limit, they will add no extra contribution to the extensional viscosity.[10] It is easy to show that the Oldroyd-B and FENE-P models differ primarily in their predictions of the steady extensional viscosities at stretch rates just above the critical coil-stretch transition rate. At steady state, the quasilinear Oldroyd-B model predicts the unphysical result that the extensional viscosity diverges at $\dot{\epsilon}_c = (1/2\tau_E)$. The FENE-P model corrects this shortcoming by incorporating the finite extensibility of the molecule (captured by a finite extensibility parameter L) into a nonlinear evolution equation for the viscoelastic stresses.[10,76] The FENE-P model predicts that the steady elongational viscosity $\eta_E(\dot{\epsilon})$ remains bounded once the chains are fully extended. The stretched chains act like an anisotropic suspension of rods with the extensional viscosity in the bulk reaching a plateau value at a high stretch rate ($\lim_{\tau_E\dot{\epsilon}\to\infty}\eta^+_E = 3\eta_s + 2(\eta_0 - \eta_s)L^2$).

The solid lines in Figure 4(a) show predictions from the FENE-P model for each liquid using the corresponding parameters $(\tau_E, \eta_s, \eta_0, L)$ from Table I. All of the ROJER data show good agreement with the predictions from the FENE-P model. The apparent viscosity extracted from the EVROC test also shows a trend that agrees qualitatively with the predictions of the

FENE-P model, but the agreement is not quantitative. The observed difference arises due to the fact that in the EVROC device material elements in different planes experience different deformation histories as they flow through the contraction/expansion. These local variations in the stretch rate of different material elements smear out the critical extension rate. By using computational shape optimization for the design and fabrication of cross-slot microfluidic devices, Haward *et al.*[32] showed that a homogeneous elongational flowfield can be achieved, by minimizing this inhomogeneity in the flow history of different material elements. Experimental results from such optimized microfluidic devices show a much better agreement with the FENE-P model.[18,32]

Figure 4(b) shows the extensional viscosities represented in dimensionless form with a Trouton ratio η_E^+/η_0 plotted as a function of the Weissenberg number $Wi = \tau_E\dot{\epsilon}$. Due to the high extensibility of the molecules ($L \sim M_w^{1-\nu}$ where ν is the solvent quality exponent[32,77]) Trouton ratios as high as $Tr \sim 1000$ can be achieved by these dilute polymer solutions at high molecular weights. These high values of the extensional viscosity can dramatically change the filament thinning dynamics at high strain rates and small length scales in a number of important application such as inkjetting, atomization, microfluidic cell sorting, etc.[6,8,58] Measurements with the EVROC device for the low viscosity solutions (green, blue, and magenta colors in Figure 3(a)) are largely polluted by nonlinear inertia effects, but Figures 4(a) and 4(b) clearly show that jetting rheometry is a reliable alternative for determining the extensional rheology of very dilute polymer solutions. The ROJER instrument not only differentiates between the extensional rheology of the different solutions in a qualitative manner (Figure 3(d)) but also quantitatively measures elongational properties in the elasto-capillary regime at constant strain rate that agree well with predictions of microstructural constitutive equations such as the FENE-P.

IV. DISCUSSION AND CONCLUSIONS

Measurements of the extensional viscosity were performed for a number of viscoelastic polymer solutions using two microfluidic test configurations; a microfabricated hyperbolic converging/diverging flow and a micromachined piezoelectric nozzle. Our results show that for dilute solutions that have both low shear viscosities and low relaxation times, the flow in the hyperbolic contraction is affected by nonlinear inertial effects before any signature of elasticity emerges. However, the EVROC is still a functional method for characterizing more viscous and more elastic solutions. The fact that many industrial and biological samples are indeed dilute solutions of large macromolecules in a low viscosity solvent encouraged us to find an alternative method for performing extensional rheometry of dilute solutions. The ROJER instrument, which is based on understanding the capillary thinning and breakup in a sub-millimeter scale physically-forced jet proves to be a valuable additional method that can discriminate between the relaxation times of the different viscoelastic solutions used in the present study. The results obtained from the ROJER and EVROC techniques also compare well with the predictions of a canonical model such as the FENE-P constitutive equation. Depending on the intrinsic properties of the specific fluid being tested, one or other of these two microfluidic rheometry methods can thus help us to determine the elongational properties of an unknown complex fluid. The question for practicing rheologists is to know where exactly are the limits and boundaries of operation for each of these two distinctly different instruments. As we show below, by knowing the intrinsic properties of a liquid we can provide guidance on deciding *a priori* which instrument to use.

A. Operating limits of the EVROC device

As we have shown in this study, the flow of a viscoelastic liquid in a microfluidic channel can be affected by three different mechanisms: elastic effects due to elongation of macromolecules passing through the contraction, viscous effects due to viscous shear stresses at the walls, and finally, adverse inertial effects due to acceleration of the material elements passing through the contraction/expansion. If we pick a characteristic length scale such as the hydraulic

diameter (denoted generically by R) for this device, we can identify three important timescales, each characterizing one of the three different aforementioned mechanisms:

$$\tau_{elas.} = \tau_E \quad : \text{Elongational relaxation time}, \tag{12a}$$

$$\tau_{visc.} = R^2\rho/\eta_0 \quad : \text{Viscous diffusion time scale}, \tag{12b}$$

$$\tau_{conv.} = R/V \quad : \text{Convective time scale}, \tag{12c}$$

where $V = Q/wh$ is the characteristic scale for the velocity in the channel. Having identified three important timescales, it is apparent that the flow of any liquid in the device can be described by two dimensionless numbers

$$\text{Reynolds Number} \quad Re = \tau_{visc.}/\tau_{conv.} = \rho VR/\eta_0, \tag{13a}$$

$$\text{Weissenberg Number} \quad Wi = \tau_{elas.}/\tau_{conv.} = \tau_E V/R. \tag{13b}$$

Equations (13a) and (13b) clearly show that for a given liquid and hyperbolic channel geometry (fixed values of τ_E, ρ, η_0, and R), changes in the flow rate lead to both Re and Wi increasing proportionally such that their ratio (given by the elasticity number[22] $El \equiv Wi/Re = \tau_E\eta_o/\rho R^2$) remains constant. In other words in the two-dimensional space spanned by Re–Wi (the operating plane for EVROC) changing the velocity corresponds physically to moving away from the origin on a line with fixed slope (or a fixed angle θ in polar coordinates) and the velocity provides a measure for the radial distance from origin (similar to r in polar coordinates). In order to observe elastic effects, and to be able to characterize them, one has to stretch the dissolved polymers sufficiently fast, compared to their relaxation rate ($V/R \geq 1/\tau_E$), or in other words, the viscoelastic timescale should dominate over the convection time scale so that the Weissenberg number of the flow is $Wi = \tau_E V/R \geq O(1)$. Thus, for any fluid with relaxation time τ_E and test geometry R, there exists a certain velocity $V_c \sim R/\tau_E$ above which the elastic effects we seek to measure begin to emerge. However, the challenge is to ensure that this (large) velocity is still small enough that the Reynolds number characterizing the flow stays lower than the critical value for onset of inertia effects (i.e., $Re = \rho VR/\eta_0 \leq O(1)$). One can easily see that by combining these two criteria then the ratio of the Weissenberg number over Reynolds number should be larger than unity; i.e., $Wi/Re \geq O(1)$. In Figure 5(a), a line of constant elasticity is shown as a dashed blue arrow in the Wi–Re plane.

The magnitude of the elasticity number thus provides a criterion for EVROC measurements. Given a specific hyperbolic channel design (i.e., a given microfluidic length scale R) and fixed liquid properties (η_0, τ_E, and ρ) one can calculate *a priori* whether the criterion for EVROC measurements (i.e., $El = \tau_E\eta_0/\rho R^2 \geq O(1)$) is satisfied or not. From this expression, it becomes apparent that in dilute polymeric liquids, such as the ones tested in this study, in which both the relaxation time and the shear viscosity are small, EVROC measurements are often impossible or contaminated by inertial effects. One possible pathway for circumventing this constraint is to fabricate even smaller microfluidic geometries (because decreasing the corresponding length scale increases the elasticity number). For the present design, the length scale is $R \equiv d_H \simeq 267\,\mu$m. However, the large pressure drop that results from very small length scales (cf. Equation (8)) can lead to fabrication failure and pumping issues. Additionally, the characteristic device length scale R cannot approach the length scale of the microstructure in the liquid, otherwise wall effects lead to hindered chain deformation and hydrodynamic screening complications.[78]

Having determined the appropriate limits of EVROC, we now consider our alternative jet-based extensional rheometer and probe the operational boundaries for the ROJER device.

B. Limits of ROJER

ROJER or other related capillary-thinning methods for extensional rheometry (such as CaBER or modified versions of CaBER[38–40]), exploit the dynamics of the Rayleigh-Plateau

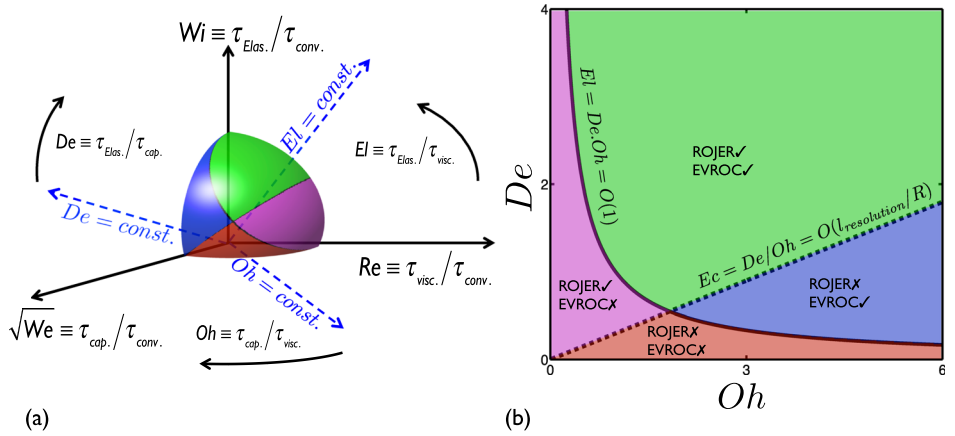

FIG. 5. (a) Measurement nomogram in 3-dimensional space for different liquids with coordinate axis x, y, z constructed from $\{\sqrt{We}, Re, Wi\}$ combination. Lines of constant elasticity El, Ohnesorge Oh and Deborah De numbers are shown by blue dashed arrows. The black arc arrows show the direction at which El, Oh and De increase in their corresponding Re–Wi, $Re - \sqrt{We}$, and $\sqrt{We} - Wi$ planes. One eighth of a unit sphere is plotted in the corner of the coordinates. Every material location in the x, y, z parameter space can be radially projected onto the surface of this sphere. Shaded colors show regions in which EVROC and the ROJER instrument can/cannot perform. (b) Measurement nomogram based on the key intrinsic properties of the fluid plotted in a 2D representation. The angular orientation of every point in the 3D parameter space sketched in (a) can be uniquely mapped onto this 2D representation (De–Oh). The solid and dashed lines are lines of constant elasticity number El and elasto-capillary number Ec, respectively. The green area indicates where both ROJER and EVROC are possible ($Ec \geq O(l_{resolution}/R)$ and $El \geq O(1)$). The magenta area is where ROJER is possible and EVROC is impossible ($Ec \geq O(l_{resolution}/R)$ and $El < O(1)$). The blue area is where ROJER is impossible and EVROC is possible ($Ec < O(l_{resolution}/R)$ and $El \geq O(1)$). The red area is where both ROJER and EVROC are not possible ($Ec < O(l_{resolution}/R)$ and $El < 1$).

instability and often rely on optical devices such as high-speed/strobe cameras, lenses and bright field illumination strategies to record the evolution in the filament diameter with time. A liquid thread with a known initial radius R that is connected at both ends to hemispherical liquid reservoirs (as in either of the ROJER/CaBER configurations) experiences higher capillary pressures inside the filament neck compared to the pressure in the hemispherical reservoirs. This pressure imbalance leads to the drainage of liquid from the filament into the reservoirs and induces an elongational flow within the filament. For a viscoelastic liquid four different physical mechanisms can be important: Elastic, viscous, and inertial effects can all play a significant role, similar to the discussion above for flow in the hyperbolic contraction. In addition to these three effects, the capillary effects play an essential role in extensional flows with free surfaces. Thus, one must consider an additional timescale that captures the effect of surface tension or capillarity in this problem,

$$\tau_{cap.} = \sqrt{\rho R^3/\sigma}: \text{ Capillary time scale.} \tag{14}$$

This capillary time scale was first introduced by Rayleigh[66,79] in his studies of liquid jets and is therefore also known as the Rayleigh time scale τ_R. It is also the timescale observed in the vibration of a liquid droplet/jet due to capillary effects.[80]

It is easy to construct an appropriate dimensionless number comparing the magnitudes of the capillary and convective timescales,

$$\sqrt{We} = \tau_{cap.}/\tau_{conv.} = V\sqrt{\rho R/\sigma}. \tag{15}$$

This ratio is the square root of the Weber number which is widely used in studies of drop/jet breakup in inkjetting and atomization operations.[81]

Thus, in ROJER, four competing timescales are involved (Equations (12) and (14)) which leads to a set of three important dimensionless numbers ($\sqrt{We}, Re, Wi$). A new coordinate $\sqrt{We}$ is therefore also required to determine the locus of each fluid being tested in the ROJER

instrument. In Figure 5(a), we represent this concept by plotting an $\{x, y, z\}$ three dimensional space with $\{\sqrt{We}, Re, Wi\}$ coordinates, respectively.

To characterize the performance of ROJER, we need to understand how the dynamics of a thinning filament are governed by the different physical mechanisms involved. Inertial effects are damped out by viscous effects if the capillary timescale is larger than the viscous diffusion time scale ($\tau_{cap.} \geq \tau_{visc.}$). The ratio of these two timescales is known as the Ohnesorge number $Oh \equiv \tau_{cap.}/\tau_{visc.} = \eta_0/\sqrt{\rho\sigma R}$ (Ref. 82) and for viscous effects to dominate over fluid inertia we require $Oh \geq O(1)$. Similarly, in order to probe viscoelastic effects in the thinning thread, the elongation rate of the filament resulting from capillary action should exceed the relaxation rate of the polymer (i.e., $1/\tau_{cap.} \geq 1/\tau_{elas.}$). The ratio of the elastic timescale to the capillary time is an intrinsic Deborah number and we thus require $De \equiv \tau_{elas.}/\tau_{cap.} = \tau_E/\sqrt{\rho R^3/\sigma} \geq O(1)$.

One additional benefit of ROJER as compared to EVROC is the fact that unlike the hyperbolic channel flow in which the characteristic length scale R is fixed and not changing with time, in ROJER the appropriate length scale $R(t)$ is evolving with time and decreases steadily from the initial value toward the final instant of breakup. By studying the functional form of the relevant dimensionless numbers such as the Deborah and Ohnesorge numbers, one can see that as $R(t)$ decreases, local estimates of the relevant force balances increase as we approach the breakup point. This means that as we follow the evolution of the thinning filament with time there exists a certain point at which elastic effects start to dominate the flow. Provided the local diameter at this crossover point is larger than the optical resolution of the setup (which we denote $l_{resolution}$), then ROJER measurements are feasible. However if this crossover point lies below our resolution limit then ROJER will not be able to resolve the elasto-capillary balance that is established close to breakup.

The practical constraints of physical optics mean that most imaging systems have a lower resolution of a few microns, $l_{resolution} \sim O(1\,\mu\text{m})$. We also know that for most complex fluids, the zero shear viscosity will not be much smaller than the viscosity of water (unless we consider supercritical solvents such as liquid CO_2). Thus, for most low viscosity liquids (with $\eta_0 \geq 10\,\text{m Pa s}$) the visco-capillary regime is accessible within the optical resolution that is achievable ($l_{resolution} \sim O(1\,\mu\text{m})$). To determine the operating boundaries of ROJER in elongational rheometry we can assume that a failed test means that elastic effects do not emerge in the thinning filament even on the finest length scale that is resolvable $R(t) \sim l_{resolution}$. In other words, even in the final moments of filament thinning the rate of stretching is not as high as the relaxation rate of the microstructure, so that $\dot{\epsilon} = (-2/R).(dR/dt) < 1/\tau_E$. If an elasto-capillary balance has not emerged yet then for most practical liquids in the final moments of thinning a visco-capillary balance starts to emerge and, consequently, the maximum rate of thinning that is optically accessible scales as $\dot{\epsilon}_{\max} \sim V_{cap.}/R \sim \sigma/\eta_0(1/l_{resolution})$. Therefore, for a viscoelastic liquid, in a device such as ROJER, to reach a critical stretch rate which is faster than the relaxation rate of the microstructure the following criteria should be met:

$$1/\tau_E \leq \dot{\epsilon}_{\max} \simeq \frac{1}{l_{resolution}}\frac{\sigma}{\eta_0} \quad \text{or} \quad \frac{l_{resolution}}{R_0} \lesssim \frac{\tau_E \sigma}{\eta_0 R_0}. \tag{16}$$

This dimensionless grouping that controls ROJER performance may be referred to as an elasto-capillary number, which can also be written in terms of De and Oh as $\tau_E\sigma/(\eta_0 R_0) = De/Oh = Ec$.[29] An alternate, easier, justification for this criterion for successful ROJER testing is to consider the stresses involved in the thinning filament. The elasto-capillary balance starts on a length scale R_{EC}, when the capillary stresses become as large as polymer elastic stresses: $\sigma/R_{EC} \sim \eta_0/\tau_E$. This simply tells us the condition for ROJER performance is $l_{resolution} \leq R_{EC} \simeq \sigma\tau_E/\eta_0$, which is equivalent to $l_{resolution}/R_0 \lesssim Ec$.

Equation (16) shows that in ROJER, just as in EVROC, the criterion for successful elongational rheometry can be expressed by a single dimensionless number based on the geometry, optical resolution and intrinsic properties of the liquid (which here includes the relaxation time, surface tension and zero shear viscosity). Combining these two separate criteria for successful

operation of the microfluidic hyperbolic channel and jet breakup measurements (EVROC and ROJER, respectively), the entire dimensionless space in Figure 5(a) can be navigated for different liquids through a two dimensional state diagram or nomogram which tells us what instrument is suitable in each region.

C. Operating nomogram for microfluidic extensional rheometry

Looking at Figure 5(a), one can see that (as we first noted for the elasticity number) both the Deborah and Ohnesorge numbers characterizing the fluid are also independent of the velocity and thus represent the slopes of rays passing through the origin and projected onto their respective $Wi - \sqrt{We}$ and $\sqrt{We} - Re$ planes. The black arcs in Figure 5(a) show the direction in which each of these dimensionless groups increase. It is also noteworthy that although the parameters $\{\sqrt{We}, Re, Wi\}$ form an independent set of coordinates, the $\{El, Oh, De\}$ set are not independent and indeed any one of the three can be expressed in terms of the other two through the relationship $El = Oh.De$. A good way to understand the difference between these two different sets of dimensionless numbers is to think of Cartesian and spherical coordinates. The dimensionless groups $\sqrt{We}, Re, Wi$ all grow linearly with velocity and thus correspond to orthogonal coordinates in Figure 5(a). In contrast El, Oh, De are all independent of velocity and represent the slopes of the position vector projected onto the three base orthogonal coordinate planes. Thus, as we increase the velocity and keep other parameters constant, we move radially away from origin on a fixed line and orientation in space. To uniquely specify a point in space using spherical coordinates, we only need two angles (θ and ϕ) and a radial distance (r) from origin. This tells us that only two dimensionless numbers from the set of El, Oh, De are needed to uniquely describe the *orientation* of any material line/vector in space. Increasing the characteristic velocity of the fluid in the device, and keeping these two angles constant, we travel on a fixed ray away from the origin. If we pick the Deborah and Ohnesorge numbers to describe the orientation of material lines then we can project our results onto the two dimensional map plotted in Figure 5(b), which is a one-to-one transform of the outer surface of the spherical segment shown in Figure 5(a).

This two-dimensional nomogram representing intrinsic viscoelastic fluid properties can help us understand where different materials are located at different length scales. For example, the abscissa ($De = 0$) corresponds to all Newtonian phenomena starting from the inviscid limit close to the origin and moving towards very viscous fluids on the far right. The region close to, but not on, the ordinate axis represents low viscosity but elastic liquids, such as the very dilute solutions of high molecular weight polymers considered in the present work. Other examples include "stringy materials" such as saliva, printing inks and paints that are often highly problematic in atomization and breakup phenomena.

The two criteria derived above for EVROC and ROJER operation can be drawn as two separate lines in this space given by the expressions $El = De.Oh = O(1)$ and $Ec = De/Oh \simeq l_{resolution}/R$ on this two dimensional plane (as shown by the solid and dashed lines in Figure 5(b)). These two lines divide the entire region into four subregions. In each of these subregions extensional rheometry with either EVROC and or ROJER may be possible depending on the values of these two groups. Different areas are shaded by different colors as follows:

(1) Green: regions in which both criteria are met ($El \geq O(1)$ and $Ec \gtrsim l_{resolution}/R$). In simple words, these fluids are both elastic and viscous enough that both ROJER and EVROC can be used for extensional rheometry.
(2) Magenta: regions in which jetting rheometry is possible but EVROC is not successful ($Ec \gtrsim l_{resolution}/R$ and $El < O(1)$). In simple words, these fluids are of such low viscosity that inertial effects dominate in the microfluidic contraction, but they are sufficiently elastic that they will form a thread during jet breakup.
(3) Blue: regions in which the criterion for EVROC is met but jetting is not possible ($El \geq O(1)$ and $Ec \lesssim l_{resolution}/R$). In simple words, these liquids are sufficiently viscous that they generate a viscoelastic contribution to the pressure drop ΔP_c across the contraction, but insufficiently elastic for the elastic stresses to balance capillary pressure in the jet until the length scale falls below the optical resolution limit.

(4) Orange: regions in which neither criterion for either EVROC or ROJER are met ($El < O(1)$ and $Ec \lesssim l_{resolution}/R$). In this region, the fluid is insufficiently viscoelastic for either class of device to operate successfully.

In studying the limits of performance for jetting rheometry, a quantitative estimate of the limiting conditions can be made by estimating the slope of the dashed line in Figure 5(b). For our ROJER system, $l_{resolution} \sim 1.5\,\mu$m and $R_0 \sim 90\,\mu$m, which shows that the actual slope of the dashed line is very small. The orange region indicated in Figure 5(b) is thus also very small and this is a very promising reason to believe that microfluidic jet breakup studies are a viable option for many dilute viscoelastic liquids. Finally, it is also necessary to point out that ROJER fails for certain liquids that are very viscous but have an extremely small relaxation time (blue region in Figure 5(b)). Examples of these liquids can be found in concentrated solutions of low molecular weight polymers which are sometimes used in food thickeners. For these liquids, the EVROC device benefits from the dominant viscous characteristics and can probe both the viscous response as well as any additional elastic contributions to the pressure drop without dealing with inertia-related issues.[56]

Our current study has examined the performance of two different microscale extensional rheometers for a set of benchmark dilute polymeric solutions. We have shown that measurements in a microfluidic hyperbolic channel can be swamped by inertial effects for sufficiently low viscosity fluids. In contrast, jet breakup studies performed with ROJER provide a promising alternate approach for elongational rheometry of these liquids. Similar efforts to explore the thinning dynamics and recoil in inkjet droplets are also being explored.[83] Using simple physical arguments, we have probed the limits of both instruments in an appropriate dimensionless operating space to construct an operational nomogram for microscale extensional rheometry. The two techniques described in the present work, used in conjunction with optimized cross-slot designs (discussed elsewhere in this special issue[18]), which enable simultaneous rheo-optical access for optically transparent materials, provide a diverse and flexible set of testing platforms for quantitative microscale extensional rheometry measurements of a wide variety of weakly viscoelastic fluids that are important in biological and industrial fields.

ACKNOWLEDGMENTS

B.K. and G.H.M. are thankful to Axalta Coating Systems for their financial support.

[1]P.-G. de Gennes, *Introduction to Polymer Dynamics* (CUP Archive, 1990), p. 57.
[2]R. G. Larson, *The Structure and Rheology of Complex Fluids* (Oxford University Press, New York, 1999).
[3]G. W. S. Blair, *An Introduction to Biorheology* (Elsevier Scientific Publ. Co., 1974), p. 215.
[4]S. Davis, Rheol. Acta **10**, 28 (1971).
[5]S. J. Haward, A. Jaishankar, M. S. N. Oliveira, M. A. Alves, and G. H. McKinley, Biomicrofluidics **7**, 044108 (2013).
[6]N. F. Morrison and O. G. Harlen, Rheol. Acta **49**, 619 (2010).
[7]B. Keshavarz, V. Sharma, E. C. Houze, M. R. Koerner, J. R. Moore, P. M. Cotts, P. Threlfall-Holmes, and G. H. McKinley, J. Non-Newtonian Fluid Mech. **222**, 171 (2015).
[8]M.-H. Wei, B. Li, R. L. A. David, S. C. Jones, V. Sarohia, J. A. Schmitigal, and J. A. Kornfield, Science **350**, 72 (2015).
[9]A. G. McDonnell, N. N. Jason, L. Y. Yeo, J. R. Friend, W. Cheng, and R. Prabhakar, Soft Matter **11**, 8076 (2015).
[10]R. B. Bird, R. C. Armstrong, and O. Hassager, *Dynamics of Polymeric Liquids*, 2nd ed. (John Wiley & Sons, New York, 1987), Vol. 1.
[11]C. J. S. Petrie, *Elongational Flows* (Pitman, London, 1979).
[12]C. J. S. Petrie, Rheol. Acta **34**, 12 (1995).
[13]C. J. S. Petrie, J. Non-Newtonian Fluid Mech. **137**, 15 (2006).
[14]M. Padmanabhan, J. Food Eng. **25**, 311 (1995).
[15]K. Walters, in *Theoretical and Applied Rheology*, edited by P. Moldenaers and R. Keunings (Elsevier, Brussels, 1992), pp. 16–23.
[16]D. F. James and K. Walters, in *Techniques in Rheological Measurement SE-2*, edited by A. A. Collyer (Springer, The Netherlands, 1993), pp. 33–53.
[17]G. H. McKinley and T. Sridhar, Annu. Rev. Fluid Mech. **34**, 375 (2002).
[18]S. J. Haward, Biomicrofluidics **10**, 043401 (2016).
[19]A. V. Bazilevsky, V. M. Entov, and A. N. Rozhkov, in *Third European Rheology Conference and Golden Jubilee Meeting of the British Society of Rheology SE-21*, edited by D. R. Oliver (Springer Netherlands, 1990) pp. 41–43.
[20]G. H. McKinley and A. Tripathi, J. Rheol. **44**, 653 (2000).
[21]L. E. Rodd, T. P. Scott, J. J. Cooper-White, and G. H. McKinley, Appl. Rheol. **15**, 12 (2005).
[22]G. H. McKinley, in *Rheology Reviews 2005* (The British Society of Rheology, 2005), ISBN:0-9547414-2-0.

[23]M. Stelter and G. Brenn, J. Rheol. **44**, 595 (2000).
[24]M. Stelter, G. Brenn, A. L. Yarin, R. P. Singh, and F. Durst, J. Rheol. **46**, 507 (2002).
[25]M. R. Duxenneuner, P. Fischer, E. J. Windhab, and J. J. Cooper-White, Biomacromolecules **9**, 2989 (2008).
[26]P. Erni, M. Varagnat, C. Clasen, J. Crest, and G. H. McKinley, Soft Matter **7**, 10889 (2011).
[27]O. Arnolds, H. Buggisch, D. Sachsenheimer, and N. Willenbacher, Rheol. Acta **49**, 1207 (2010).
[28]W. Mathues, C. McIlroy, O. G. Harlen, and C. Clasen, Phys. Fluids **27**, 093301 (2015).
[29]G. H. McKinley, SOR Bull. **74**(2), 6–9 (2005).
[30]F. J. Galindo-Rosales, M. A. Alves, and M. S. N. Oliveira, Microfluid. Nanofluid. **14**, 1 (2013).
[31]S. J. Haward, J. A. Odell, Z. Li, and X.-F. Yuan, Rheol. Acta **49**, 633 (2010).
[32]S. J. Haward, M. S. N. Oliveira, M. A. Alves, and G. H. McKinley, Phys. Rev. Lett. **109**, 128301 (2012).
[33]P. E. Arratia, J. P. Gollub, and D. J. Durian, Phys. Rev. E **77**, 036309 (2008).
[34]S. L. Anna, N. Bontoux, and H. A. Stone, Appl. Phys. Lett. **82**, 364 (2003).
[35]S. L. Anna and H. C. Mayer, Phys. Fluids **18**, 121512 (2006).
[36]B. Steinhaus, A. Q. Shen, and R. Sureshkumar, Phys. Fluids **19**, 073103 (2007).
[37]I. Cohen and S. R. Nagel, Phys. Fluids **13**, 3533 (2001).
[38]L. Campo-Deaño and C. Clasen, J. Non-Newtonian Fluid Mech. **165**, 1688 (2010).
[39]D. C. Vadillo, J. Rheol. **54**, 261 (2010).
[40]D. C. Vadillo, W. Mathues, and C. Clasen, Rheol. Acta **51**, 755 (2012).
[41]P. Schümmer and K. H. Tebel, Rheol. Acta **21**, 514 (1982).
[42]P. Schümmer and K. H. Tebel, J. Rheol. **26**, 77 (1982).
[43]P. Schümmer and K. H. Tebel, J. Non-Newtonian Fluid Mech. **12**, 331 (1983).
[44]C. J. Pipe and G. H. McKinley, Mech. Res. Commun. **36**, 110 (2009).
[45]E. B. Adams, J. C. Whitehead, and D. C. Bogue, AIChE J. **11**, 1026 (1965).
[46]F. N. Cogswell, Polym. Eng. Sci. **12**, 64 (1972).
[47]F. N. Cogswell, J. Non-Newtonian Fluid Mech. **4**, 23 (1978).
[48]A. E. Everage and R. L. Ballman, Nature **273**, 213 (1978).
[49]D. Binding and K. Walters, J. Non-Newtonian Fluid Mech. **30**, 233 (1988).
[50]D. F. James and J. H. Saringer, J. Non-Newtonian Fluid Mech. **11**, 317 (1982).
[51]G. H. McKinley, W. P. Raiford, R. A. Brown, and R. C. Armstrong, J. Fluid Mech. **223**, 411 (1991).
[52]M. S. N. Oliveira, M. A. Alves, F. T. Pinho, and G. H. McKinley, Exp. Fluids **43**, 437–451 (2007).
[53]L. Campo-Deaño, F. J. Galindo-Rosales, F. T. Pinho, M. A. Alves, and M. S. Oliveira, J. Non-Newtonian Fluid Mech. **166**, 1286 (2011).
[54]M. Nyström, H. R. Tamaddon Jahromi, M. Stading, and M. F. Webster, Rheol. Acta **51**, 713 (2012).
[55]P. C. Sousa, F. T. Pinho, M. S. N. Oliveira, and M. A. Alves, Biomicrofluidics **5**, 14108 (2011).
[56]T. J. Ober, S. J. Haward, C. J. Pipe, J. Soulages, and G. H. McKinley, Rheol. Acta **52**, 529 (2013).
[57]G. H. McKinley, L. E. Rodd, M. S. N. Oliverira, and J. Cooper-White, J. Cent. South Univ. Technol. **14**, 6–9 (2007).
[58]E. J. Lim, T. J. Ober, J. F. Edd, S. P. Desai, D. Neal, K. W. Bong, P. S. Doyle, G. H. McKinley, and M. Toner, Nat. Commun. **5**, 4120 (2014).
[59]G. D'Avino, G. Romeo, M. M. Villone, F. Greco, P. A. Netti, and P. L. Maffettone, Lab Chip **12**, 1638 (2012).
[60]A. M. Leshansky, A. Bransky, N. Korin, and U. Dinnar, Phys. Rev. Lett. **98**, 234501 (2007).
[61]S. Yang, J. Y. Kim, S. J. Lee, S. S. Lee, and J. M. Kim, Lab Chip **11**, 266 (2011).
[62]K. Kang, S. S. Lee, K. Hyun, S. J. Lee, and J. M. Kim, Nat. Commun. **4**, 2567 (2013).
[63]B. R. Elbing, E. S. Winkel, M. J. Solomon, and S. L. Ceccio, Exp. Fluids **47**, 1033 (2009).
[64]C. J. Pipe, T. S. Majmudar, and G. H. McKinley, Rheol. Acta **47**, 621 (2008).
[65]J. Plateau, Ann. Phys. Chem. **156**, 566 (1850).
[66]L. Rayleigh, Proc. London Math. Soc. **10**, 4 (1878).
[67]G. Brenn, Z. B. Liu, and F. Durst, Int. J. Multiphase Flow **26**, 1621 (2000).
[68]A. V. Bazilevskii, V. M. Entov, and A. N. Rozhkov, Polym. Sci. Ser. A **43**, 716 (2001).
[69]C. W. Macosko, *Rheology: Principles, Measurements and Applications* (VCH Publishers Inc, New York, 1994).
[70]L. E. Rodd, T. P. Scott, D. V. Boger, J. J. Cooper-White, and G. H. McKinley, J. Non-Newtonian Fluid Mech. **129**, 1 (2005).
[71]L. E. Rodd, J. J. Cooper-White, D. V. Boger, and G. H. McKinley, J. Non-Newtonian Fluid Mech. **143**, 170 (2007).
[72]See supplementary material at http://dx.doi.org/10.1063/1.4948235 for a more detailed description of the ROJER measurements.
[73]J. R. Collier, O. Romanoschi, and S. Petrovan, J. Appl. Polym. Sci. **69**, 2357 (1998).
[74]In calculating the extension rates for both Figures 4(a) and 4(b) we multiplied the stretch rates calculated from Equation (10) by a factor of 0.75 ($\dot{\epsilon} = (3/4)\dot{\epsilon}_p$). This factor comes from the fact that the stretch rate in the elasto-capillary balance plateaus around a critical value $\dot{\epsilon}_p = 2/3\tau_E$ while the predictions for elongational viscosity from constitutive equations such as Oldroyd-B/FENE-P show that the coil-stretch transition happens at a lower critical strain rate $\dot{\epsilon}_c = 1/2\tau_E$. In order to make a quantitative one-to-one comparison between the ROJER data and known constitutive equations all the stretch rate data from ROJER for each of the test fluids were multiplied by $(1/2)/(3/2) = 3/4$.
[75]A. Peterlin, J. Polym. Sci., Part B **4**, 287 (1966).
[76]L. E. Wedgewood, D. N. Ostrov, and R. Bird, J. Non-Newtonian Fluid Mech. **40**, 119 (1991).
[77]M. S. N. Oliveira and G. H. McKinley, Phys. Fluids **17**, 071704 (2005).
[78]D. J. Mai, C. Brockman, and C. M. Schroeder, Soft Matter **8**, 10560 (2012).
[79]L. Rayleigh, Proc. R. Soc. London **29**, 71 (1879).
[80]S. H. Lamb, *Hydrodynamics* (Courier Corporation, 1945), p. 738.
[81]A. H. Lefebvre, *Atomization and Sprays* (Hemisphere Publishing Corporation, 1989), p. 421.
[82]G. H. McKinley and M. Renardy, Phys. Fluids **23**, 127101 (2011).
[83]H. Staat, A. van der Bos, M. van den Berg, H. Reinten, H. Wijshoff, M. Versluis, and D. Lohse, Bull. Am. Phys. Soc. **60** (2015); available at http://meetings.aps.org/link/BAPS.2015.DFD.L35.8.